

## Author's response to reviewer's comments:

We would like to thank all the reviewers for their many constructive comments and for their unanimous support in publishing the manuscript. Below, we listed the comments from all three reviews, [our response](#), and [changes in the manuscript](#). In some cases, manuscript changes are only referred by their position in the manuscript, while for the case of minor changes (i.e. spelling, wording), these are only [confirmed](#). The LaTeX manuscript has been updated with the package “changes”, i.e. added, deleted, and replaced text is marked as such.

### Reviewer1

Review of "Impact of particle shape on the morphology of noctilucent clouds" by J. Kiliani et al.

#### General Comments

This paper describes the impact of non-spherical ice particles in NLC simulations, addressing both the microphysical and optical properties. While many previous studies have looked at the optical effects resulting from non-spherical ice, the present study is novel in that it simulates the impact of non-spherical ice on NLC microphysics as well. The results are applicable to ACP and are for the most part clearly presented. The results support the conclusions, the abstract, and the figures and citations are appropriate. I recommend that this paper be published after the concerns below are addressed.

#### Specific Comments

1) It is interesting that cylinders give greater backscatter than spheres in the simulations. There is an important question, however, that is not currently addressed: is this due to greater ice mass density ( $m$ ), optical effects, or both? This is an important point in the interpretation, i.e., is higher backscatter simply higher  $m$ , or can it go the other way? Understanding this aspect of the results could lead to very different interpretation of the lidar measurements. For example if all the curves in Fig. 7 have the same  $m$  vs. altitude, then determining  $m$  from a given backscatter observation depends heavily on knowledge of the particle shape. Additionally, many instruments can only infer NLC mass-related properties (e.g., IWC), and thus attempts at relating the lidar to these instruments could be affected. I recommend including a second panel in Fig. 7 that shows the  $m$  versus altitude for each model case (or add this panel to Fig. 8).

We have added a panel of ice mass density for Fig. 7. The figure caption has been extended to include this, and also to further specify the data used for the figure:

Average NLC parameters north of  $60^\circ$  N during July of 2009, from the reference simulation (spherical particles) and 6 sensitivity runs with different distributions of cylindrical particles Left panel: backscatter coefficient (532 nm), right panel: ice mass density ( $\text{g}/\text{km}^3$ ). No threshold is used, i.e. zero values are included in the average.

To describe the additional panel, we also added this to the second paragraph in Sec. 3.2:

The ice mass density of NLC in simulations with cylindrical particles is also up to ~30 % higher than in the spherical particle run. As for the backscatter coefficient, the increase in ice mass is larger for simulations with disc shaped cylinders than for needle shapes. The rather low values in average brightness and ice mass density result from the lack of a threshold. As minor changes in the mass density make some populations of clouds fall below the threshold in one simulation or the other, omitting a threshold gives more accurate comparisons for the different model runs. Additionally, we updated the statement about IWC in the conclusions to reflect this.

2) A very important aspect of this study is how the new results for non-spherical ice may change the interpretation of observations. To this end, it would be useful to estimate what changes would be expected in the particle size and IWC determined from lidar (e.g., do the inferred radii and IWC increase or decrease and by how much). In addition, the information in Fig 9 seems like it would be important for other investigators who would like to consider your results. For example, is it possible to parameterize these probabilities in order to capture your shape distributions in the forward model of some other instrument? While this may be outside the scope of your paper, it is the kind of information others would appreciate.

We see the benefit of the suggestions and agree that a parametrization of shape of the axis ratio distribution as a function of  $r$  is beyond the scope of the paper.

The implications for the lidar size retrieval (not shown in the current paper) are likely small.

The retrieval algorithm (described in Baumgarten, ASR, 2007) already makes use of the optical effects of non-spherical particles with a uniform shape distribution of 0.1 to 10.0. To quantify expected (small) effects a parametrization of the axis ratio distribution as function of  $r$  is needed.

We have extended the manuscript in section 2.3 to make clear that the lidar size retrieval uses a uniform distribution of AR between 0.1 and 10.

3) There has been a debate of sorts in the NLC community concerning particle shape. In particular Rapp et al [2007] used the ALOMAR lidar data with modeling to arrive at axial ratios of ~5, while many satellite experiments indicate values of around 2. The present study now uses the ALOMAR data with more advanced modeling to arrive at axial ratios of ~2.4. You should discuss the differences and acknowledge the changes in your results from the Rapp et al. paper (probably in the conclusions).

The ALOMAR lidar data shown in Rapp et al. [2007] are 11 measurements in Summer 1998.

Rapp et al. [2007] used only mean CR for comparison and investigated only a limited set of fixed axis ratios. They discussed that AR 1/5 and 7 are best matches. In this study, we used 30000 measurements between 1998 and 2014 and found that the most robust way of comparing model to observations is by using the full CR distribution. Furthermore our modeling shows that we have to use a distribution of axial ratios instead of single axial ratios as in Rapp et al. [2007].

We summarize the Rapp07 results in the conclusions and discuss the improvements with our new results:

Rapp et al. [2007] found that color ratios from NLC as measured by lidar do not match the model simulation well if it is assumed that particles are of spherical shape. For 11 color ratio measurements in 1998 by von Cossart [1999] they found that needles with axial ratios of 1/5 or plates with axial ratio of 7 explain the observations.

## Technical Corrections

1) Throughout: "Figure" and "Fig." are used alternately, be consistent with the style specified by the Journal.

Done

2) Abstract, line 5: State here that the modeling of cylinders was both microphysical and optical.

Done

3) Abstract, line 10: State that the relative probability of certain shapes is determined by the model (I believe this is the case), which is important because it is based on the microphysics and not an assumption.

The model does not directly give probabilities of certain shapes, only indirectly by comparing optical signals. The large parameter space of possible shape distributions does not allow a more direct approach. We considered this too complex for the abstract, unless there is some compact way of rephrasing.

4) Abstract, line 11: Please define "stronger". Is this greater mass density, or greater lidar backscatter, or both?

Backscatter signal, we elaborated and also included the change in mass density.

5) 16020, line 22: "validated" should be "inferred"

Done

6) Section 1: It would be useful here to include a brief summary of the axial ratios reported by previous authors, for example, Baumgarten et al. [2002] indicate  $\epsilon < 2.5$ , Eremenko et al. [2005] indicate  $\epsilon \sim 2$ , Rapp et al. [2007] determined  $\epsilon$  of  $\sim 5$  or  $0.2$ , etc...

We extended the introduction accordingly:

For example Baumgarten et al. [2002] indicate needle like particles with a diameter over length ratio ( $\epsilon$ ) of less than 0.4, Eremenko et al. [2005] indicate needle or plate like particles with  $\epsilon \sim 0.5$  or  $\epsilon \sim 2$ . Rapp et al. [2007] estimated  $\epsilon \sim 0.2$  or  $\epsilon \sim 7$ . The most extensive data set is from the SOFIE (Solar Occultation For Ice Experiment) instrument, with mean  $\epsilon \sim 0.5$  or  $\epsilon \sim 2$  (Hervig et al. [2009], Hervig and Gordley [2010]).

7) 16021, line 14: "to NLC" should be "in"

Done

8) 16022, line 5: sentence "r is the..." is redundant to previous statement.

We removed the sentence.

9) 16022, line 7: You keep the particle axial ratio constant during growth or sublimation. However, if ice accumulates uniformly on a cylinder, the axial ratio will change. For example, consider an initial length = 10 and diameter = 20 nm ( $\epsilon = 2.0$ ), adding a 10 nm layer of ice uniformly to the sides and ends gives  $\epsilon = 1.5$ . While this example may be overly simplistic, it indicates that particles become less asymmetric as they grow. You should discuss this possibility and also review the growth of asymmetric particles (which borrows from electrostatic theory, i.e., think of the magnetic field lines surrounding a polarized rod).

We agree that the assumption of constant axial ratio during growth and sublimation is a simplification. It was chosen here to allow formation of large particles with high axis ratios without greatly increasing the complexity of the microphysical model. We included a paragraph in the discussion to discuss this: This last assumption was chosen as a simple way to treat axis ratios effects on the microphysics. Uniform condensation on an elongated or flattened particle would continually decrease its axial ratio during growth. On the other hand the crystalline structure of ice or particle charge could counteract this to increase axial ratios. An implementation of all effects would require much more complex microphysics, which is beyond the scope of the paper.

10) 16024, line 10 (and elsewhere): "number density" is typically used in reference to gas molecules, "concentration" is the term generally used to describe the number of aerosols in a volume of air.

We prefer to use number density as concentration is misleading. See [http://en.wikipedia.org/wiki/Number\\_density](http://en.wikipedia.org/wiki/Number_density): The number density of solute molecules in a solvent is sometimes called concentration, although usually concentration is expressed as a number of moles per unit volume (and thus called molar concentration).

11) 16024, line 12: define the acronym "CR"  
The acronym is already defined in Line 7.

12) 16024, line 22: insert "(Figure 3)" at the end of this sentence.  
We inserted a reference in the beginning of the sentence.

13) Figure 3: The numbers in color (presumably radii) need to be described in the caption. The caption should indicate that these results are simulations. The curves in this figure are not easy to understand, and you need to add statements in the caption that help the reader in this regard. For example the oscillating colored lines are confusing, what causes this modulation? Also, what changes along the (grey scale) solid, dot, and dash lines? I assume it is particle size but you need to clearly describe this in the caption. Does  $\epsilon = 1$  refer to spheres or cylinders? Are all the results for cylinders? I ask because the text says Fig. 3 is for cylinders, but Fig. 4 says there are results in Fig 3 for spheres. The caption should state all relevant information. Many of the above comments apply to other figures as well.

We enhanced the figure caption to address these points (also by other reviewers): Combinations of color ratios UV/Vis (355/532 nm) and IR/Vis (1064/532 nm) for different particle equivalent radii ( $r$ ) and axis ratios ( $\epsilon$ ), as calculated from Mie theory for cylindrical particles. Colored solid lines show constant  $r$  with variable  $\epsilon$ , the equivalent radius in nm is shown by the numbers near the  $\epsilon = 1$  position (the line inflection is caused by very small  $d\beta/d\epsilon$  at  $\epsilon = 1$ ). Line oscillations, mainly along the  $\epsilon < 1$  branch, stem from rounding errors in the Mie scattering tables. The grey scale lines (dotted/dashed) show variable  $r$  for fixed axis ratios, including cylinders with  $\epsilon = 1$  for the solid black line.

The caption of Fig. 4 was also modified, we added:  
These are very similar but not identical to the  $\epsilon = 1$  cylinders in Fig. 3.

14) 16024, line 22: This sentence needs clarification: "Since small particles (i.e.,  $r < \sim XX$  nm) are difficult to detect by lidar, having similar..."

We inserted a radius threshold (15 nm)

15) 16024, line 27: "UV/Vis" should be "the UV/VIS ratio".

Done

16) 16025, line 1: "particles up to" should be "particles with radii up to".

Done

17) 16024 & 16025: This discussion needs to refer to Figure 3 more often, that is, let the reader know when a statement is illustrated in the Figure.

We added two references to Fig. 3.

18) 16025: lines 15-25: Did the model runs for various particle shape use the exact same atmospheric conditions (e.g., T, H<sub>2</sub>O, winds)? Please clarify this aspect of the simulations.

We clarified in the manuscript that exactly the same atmospheric conditions were used.

19) 16026, line 15-16: This sentence needs to be reworded.

We rephrased it to

Fig. 4 shows the effect of the smoothing filter on the modeled color ratios for a simulation containing both needle- and disc-shaped particles.

20) Figure 5: State the details for the observations used: the latitude, years, days of year, and altitudes (were these at the altitude of max backscatter?). What are the numbers (20, 40, 60, 80, 100, 120) in the figure? What is chi squared = 54.53 referring to (you describe this after discussing Fig 5)? "only spheres" should be "simulation for spheres", or, remove it from the Figure because the caption states this. It is hard to discern color for the model contours.

We included additional information on the data used for Figs. 4, 5, and 6 in paragraphs 1 and 3 of Sec. 3.1. The numbers refer to color ratios for spherical particles, see Fig. 4, this applies to Fig. 6 as well. We included a reference to Fig. 6 regarding  $\chi^2$ , and changed the Text within the Fig. 5 to "simulation for spheres".

21) Figure 6: The model result contours are hard to see, can the lines be thicker?

We have tried different presentations but came to the conclusion that the current presentation is showing the key results.

22) 16028: These paragraphs are somewhat tedious in that they spend much of the readers time reiterating what can be seen in Fig. 6. This section could be reworded to arrive at the punch line, which is that one of the cases gives the best re-production of the observations, telling us the reasons for this agreement. In addition, the text refers to the simulations as "(b)" or "(e)", which seems to be the corresponding panel in Fig. 6. The correct way would be to either cite the Figure completely, e.g., "the results in Fig 6b", or to previously define model runs as a through f (for example in 16025 lines 21-25), and subsequently refer to "scenario a" or "model a". In either case it would be useful to occasionally remind the reader what scenarios a - f are.

We agree that the paragraph is difficult to read but think that shortening this section is not helpful. This section leads up to the core statement of the article, i.e. which axis ratios are supported by measurements. Since the parameter space of possible axis ratio distribution is so large, we considered it relevant to describe in detail how both mode position and tail shape are compared for multiple simulations.

We improved the paragraph and clarified that the simulation number refers to the corresponding panel in Fig. 6.

23) 16028, line 27 "extend" should be "extent".

Done

24) 16029, line 10: state here that Fig 7 shows simulations.

Done, also reworded the sentence because of the additional panel in Fig 7:

...we compare observable parameters of simulated NLC layers...

25) 16030, line20: "growing visible" do you mean "growing to sizes that are visible to lidar" or "to human eyes"? Perhaps simply state to  $r > XX$  nm.

Done

26) 16030, line 23: "r5-6" should be "r5 to r6".

Done

27) Table 2: It would be instructive to add a column for the ratio of IWC / Bint for all the cases. This will help in addressing the concerns in Specific Comment #2 above.

We addressed comment #2 by adding a panel with IWC to Fig. 7.

The ratio of IWC/Bint is misleading from our point of view as it depends on particle shape but also (and more importantly) on the combination of n,r and distribution width.

28) Figure 8: Caption should state that these are model results. Also please clarify what equivalent radius is.

Done, we changed the caption to

Simulated volume equivalent radius...

29) 16031, line 4: Please elaborate on what is meant by improved growth conditions.

We changed the phrasing and added:

...during strong growth conditions, i.e. when temperatures are low enough that a high fraction of the water vapor within the growth region is depleted by particle growth.

30) 16031, line 9: Please quantify "brighter" (in % preferably).

Done

31) 16031, line 10: The distributions in Fig. 9 are rather interesting, in that I assume they develop in the model due to growth rates and fall speeds varying in axial ratio. If this is correct, then the text should discuss this point. Is the initial shape distribution in the

model a flat line (same number of particles in each  $\epsilon$  bin)? Please clarify.

Yes, the initial distribution is uniform in  $\log \epsilon$ , this is stated earlier in Sec. 3.1., Paragraph 2. We adapted the next sentence to clarify:

When counting all particles, the uniform initial distribution shapes (see Sect. 3.1) within...

The impact of growth rates and fall speeds on ice particle development is discussed later in the section.

32) Figure 9: The inset text is small and difficult to read. While the specific classes of particle shape can be found in Fig 6, this is tedious to transfer, and it would help to repeat the information here. Do not plot the zero values, which results in the near-vertical lines at the termination of a curve. Finally, the y-axis notation of "[% max]" is cryptic, "normalized probability (%)" would be better.

We changed the figure as suggested, but prefer to keep the mean axial ratio values given in the figure.

33) 16031: This discussion needs to refer to Fig 9 more specifically (e.g., Fig 9d, etc...) and more frequently, to aid in understanding the results.

We added two references to Fig. 9 in the discussion.

34) 16031, lines 15-23: These statements seem to be important, that is, the model indicates that elongated shapes are much more common than spherical shapes. It would add to the paper if you discuss the reasons for this in more detail. For example, is it because of the increased growth rate, or reduced fall speeds, or both?

We briefly discuss this in the next paragraph, where we added a sentence to include our opinion on the contributions of growth rate / sedimentation:

The prevalence of high axis ratios among large particles is most likely due to the increased growth rates, with the reduced fall speed contributing slightly at most. Otherwise we would expect the center of the U-shape shifted to elongated particles, like for the correction factor  $\Phi_{\text{sedi}}$ , see Fig. 2.

We also revised a statement in the first paragraph of Sect 3.2:

This disparity is caused by the stronger microphysical effects on growth and sedimentation for disc shapes as compared to needles

35) 16032, line 21: Elaborate on what "nearly perfect conditions" means.

We shortened the text since a discussion of the operational reasons for not performing the measurements routinely would distract from the main message of the paper.

36) 16033, line 2: what is the standard deviation of the mean  $\epsilon$ ? In determining the average of values  $<1$  and  $>1$ , did you do anything to the values  $<1$ , for instance use them as  $1/\epsilon$  when computing the average?

We added a note how the mean  $\epsilon$  is calculated in section 3.2:

Fig. 9 includes the average axis ratio  $\langle \epsilon \rangle$  for each radius threshold, calculated using  $1/\epsilon$  for  $\epsilon < 1$ .

## Reviewer2

### GENERAL COMMENTS

This paper addresses the issue of ice particle shape effect on noctilucent cloud (NLC) behavior by implementing different combinations of shapes in microphysical model calculations, evolving a population of ice particles using a 3-D atmospheric model, and determining the impact on observable NLC properties. These results are then compared to multi-wavelength lidar measurements that provide information on ice particle size and shape distributions.

The 3-D atmospheric model used in this study (MIMAS) is an extension of the LIMA-ICE model described in previous papers, and the issues associated with introducing non-spherical ice particles are carefully described. The implications of particle shape for the “color ratio” of scattering intensity between two different wavelengths are also presented. This discussion provides a framework for interpreting the lidar measurements. The analysis of ALOMAR lidar observations explains in detail which combination of particle shapes is most effective in matching the data. The impact of non-spherical ice particle shapes on larger scale ice layer properties typically derived from satellite measurements is also discussed.

This paper is very thorough and well-written. A few specific comments are listed below.

### SPECIFIC COMMENTS

p. 16023, lines 2-4: This is a good example of the clear summary statements for key results that appear throughout this paper.

Thank you.

p. 16024, lines 13-15: It is not clear to this reviewer why each of the colored solid curves for different equivalent radii in Figure 3 all have inflection points that lie on the  $\epsilon = 1$  curve.

We have extended the caption of Fig. 3 to make these points (also by other reviewers) clearer: Combinations of color ratios UV/Vis (355/532 nm) and IR/Vis (1064/532 nm) for different particle equivalent radii ( $r$ ) and axis ratios ( $\epsilon$ ), as calculated from Mie theory for cylindrical particles. Colored solid lines show constant  $r$  with variable  $\epsilon$ , the equivalent radius in nm is shown by the numbers near the  $\epsilon = 1$  position (the line inflection is caused by very small  $d\beta/d\epsilon$  at  $\epsilon = 1$ ). Line oscillations, mainly along the  $\epsilon < 1$  branch, stem from rounding errors in the Mie scattering tables. The grey scale lines (dotted/dashed) show variable  $r$  for fixed axis ratios, including cylinders with  $\epsilon = 1$  for the solid black line.

p. 16026, lines 5-6: Any specific reason for using only strong NLC detections? Just to have more confidence in color ratio results?

A deviation of the shape from spheres is more easily detectable for larger particles, small particles look like spheres if the wavelength of the light is too large. This is why the lines meet at the Rayleigh Point.

We have added this explanation to Sec. 2.3, paragraph 3:

This makes analyzing particle shape using color ratios much more feasible for large particles, which primarily occur in bright ice clouds.

and referenced it in Sec. 3.1, paragraph 3.

### TECHNICAL CORRECTIONS

p. 16028, line 13: “prelimiary” should be ‘preliminary’.

Done

p. 16028, line 27: “extend” should be ‘extent’.

Done

p. 16033, line 1: “best” should be ‘most’?

Done

### Reviewer3

#### General comments:

This article studies the effect of non-spherical (cylindrical) as compared to spherical particles in Noctilucent clouds (NLC), which is what models generally assume. The growth rate and the fall speed of the particles in the model (MIMAS, formerly known as LIMA/ICE) as well as the optical properties of the particles are adjusted to account for cylindrical particles. The scattering properties of the modeled clouds are then compared to 3 color measurements by the ALOMAR RMR-Lidar. The best agreement is found when there is a mix of needle and disk shaped particles with an axis ratio of 2.8. This piece of work is important for the community and should definitely be published. However, I have one major comment that I believe the authors should address before publication.

I am missing a sensitivity study and discussion of if other cloud properties, i.e. apart from the shape, could be adjusted to give color ratios that agree better with the Lidar measurements. This is important, because the paper as it reads now, demonstrates that the particles in general are not spherical (at least not the majority of them). Before stating that I believe it is important to investigate if spherical particles could somehow “do the job”.

It has been shown by measurements (Baumgarten, Eremenko, Hervig) that the particles are non-spherical. The paper investigates the effect of non-spherical particles on the morphology of the clouds. The comparison to the lidar is to show that the model results actually agree to observations. We have clarified this in the introduction of the manuscript:

For example Baumgarten et al. (2002) indicate needle like particles with a diameter over length ratio ( $\epsilon$ ) of less than 0.4, (Eremenko et al., 2005) indicate needle or plate like particles with  $\epsilon \approx 0.5$  or  $\epsilon \approx 2$ . Rapp et al. [2007] estimated  $\epsilon \approx 0.2$  or  $\epsilon \approx 7$ . The most extensive data set comes from the SOFIE (Solar Occultation For Ice Experiment) instrument, with mean  $\epsilon \approx 0.5$  or  $\epsilon \approx 2$  (Hervig et al., 2009a; Hervig and Gordley, 2010).

Especially since you have added two or three (?) more degrees of freedom when you add the axis ratio and the proportion of particles that have each axis ratio. By adding more degrees of freedom you can expect a somewhat better agreement to any result. Other properties that I can think of which may or may not affect the color ratios (apart from axis ratio) include the amount of water vapor, the temperature and vertical (and perhaps even horizontal) wind.

We agree that the environmental conditions play an important role for the morphology and microphysical properties of NLC.

In order to include a wide variety of environmental conditions (temperature, water vapor, vertical and horizontal winds) we have used several days of model simulations of NLC in the northern hemisphere. We added to the manuscript:

All simulations used exactly the same atmospheric conditions (e.g. temperature, H<sub>2</sub>O, wind).

Another property that in my view is very likely to be important, but that may be difficult to investigate, is the non-purity of the ice, such the mixture of meteoric material into the ice (see Hervig et al, The content and composition of meteoric smoke in mesospheric ice particles from SOFIE observations, JASTP, v 84-86, 2012, p1-6). Even if it is beyond the scope of the manuscript to properly investigate

the effect of non-pure ice, it should be discussed.

The smoke contribution plays a minor role as its volumetric fraction is low. Assuming a 3 nm smoke core in a 50 nm ice particle gives a volumetric fraction of  $2e-4$ . So we expect no huge effect on the NLC. We cannot exclude an effect on speed of sedimentation for small particles (10 nm?)

As a more minor comment I further believe the model adjustments, while well described in parts, should be summarized better. What is actually adjusted to take the cylindrical particles into account? Is it only equation 1, 3 and the T matrix? If so please summarize that.

Yes that is accurate, we included this as a summary at the end of Sect. 2.1:

In summary, modeling of non-spherical particles is implemented by adjusting growth rate (Equation 1), fall speed (Equation 3), and Mie scatter coefficient using the T-matrix method.

Moreover, at the bottom of page 16023 it states that the standard version of MIMAS only calculates backscatter ratios for 532 nm. It does not say if this has been modified in the new version. I assume it has, because if not I do not see how you can calculate the color ratios. Please state this if it is the case.

We improved the MIMAS description accordingly.

#### **Specific comments:**

P 16023, line 21: 'scatters light' should probably be 'back scatters light', unless they scatter less efficiently in all directions.

Yes; we changed the text accordingly.

P 16029, line 23: I assume  $\beta_{max}$  in the maximum brightness, not the maximum column brightness.

Yes; we changed the text accordingly.

Figure 3: This figure needs to be improved. Are the gray/black lines referring to spherical particles only? Why do not all colored lines have two dashed, one solid and two dotted lines? I.e. one for each radius and disk shape. Moreover, describe in the caption what the colors are. I assume they are equivalent radius in nanometers.

We enhanced the figure caption to address these points (also by other reviewers):

Combinations of color ratios UV/Vis (355/532 nm) and IR/Vis (1064/532 nm) for different particle equivalent radii ( $r$ ) and axis ratios ( $\epsilon$ ), as calculated from Mie theory for cylindrical particles. Colored solid lines show constant  $r$  with variable  $\epsilon$ , the equivalent radius in nm is shown by the numbers near the  $\epsilon = 1$  position (the line inflection is caused by very small  $d\beta/d\epsilon$  at  $\epsilon = 1$ ). Line oscillations, mainly along the  $\epsilon < 1$  branch, stem from rounding errors in the Mie scattering tables. The grey scale lines (dotted/dashed) show variable  $r$  for fixed axis ratios, including cylinders with  $\epsilon = 1$  for the solid black line.

Manuscript prepared for Atmos. Chem. Phys. Discuss.  
with version 2015/04/24 7.83 Copernicus papers of the L<sup>A</sup>T<sub>E</sub>X class copernicus.cls.  
Date: 28 September 2015

# Impact of particle shape on the morphology of noctilucent clouds

**J. Kiliani, G. Baumgarten, F.-J. Lübken, and U. Berger**

Leibniz-Institute of Atmospheric Physics at Rostock University, Schlossstraße 6, 18225  
Kühlungsborn, Germany

Correspondence to: G. Baumgarten (baumgarten@iap-kborn.de)

Discussion Paper

Discussion Paper

Discussion Paper

Discussion Paper

## Abstract

Noctilucent clouds (NLC) occur during summer in the polar region at altitudes around 83 km. They consist of ice particles with a typical size around 50 nm. The shape of NLC particles is less well known, but important both for interpreting optical measurements and modeling ice cloud characteristics. In this paper, NLC modeling of [microphysics and optics](#) is adapted to use cylindrical instead of spherical particle shape. The optical properties of the resulting ice clouds are compared directly to NLC 3-color measurements by the ALOMAR RMR-Lidar between 1998 and 2014. Shape distributions including both needle- and disc-shaped particles are consistent with lidar measurements. The best agreement occurs if disc shapes are 60 % more common than needles, with a mean axis ratio of 2.8. Cylindrical particles cause stronger ice clouds on average than spherical shapes [with an increase of backscatter at 532 nm](#) by  $\approx 30\%$  [and about 20 % in ice mass density](#). This difference is less pronounced for bright than for weak ice clouds. Cylindrical shapes also cause NLC to have larger but a smaller number of ice particles than for spherical shapes.

## 1 Introduction

Noctilucent clouds (NLC), also called polar mesospheric clouds (PMC), occur in the polar region at altitudes around 83 km. NLC only form during summer, when the upper mesosphere is coldest (below 130 K) and the amount of water vapor is enhanced due to transport by atmospheric circulation (Holton, 1983). NLC consist of ice particles with  $r \approx 50$  nm which form by heterogeneous nucleation, for example around meteoric dust particles (Turco et al., 1982).

The size of mesospheric ice particles can be [inferred/validated](#) with optical instruments such as lidar (Light Detection And Ranging), which measure backscattered light at multiple wavelengths. Using microphysical modeling in this context requires simulating particle shape, since measurements indicate that NLC particles in general are not spherical

Baumgarten et al., 2002; Eremenko et al., 2005; Baumgarten and Thomas, 2006; Rapp et al., 2007; Hervig et al., 2009a; Hervig and Gordley, 2010).

For example Baumgarten et al. (2002) indicate needle like particles with a diameter over length ratio ( $\varepsilon$ ) of less than 0.4, (Eremenko et al., 2005) indicate needle or plate like particles with  $\varepsilon \approx 0.5$  or  $\varepsilon \approx 2$ . Rapp et al. (2007) estimated  $\varepsilon \approx 0.2$  or  $\varepsilon \approx 7$ . The most extensive data set is from the SOFIE (Solar Occultation For Ice Experiment) instrument, with mean  $\varepsilon \approx 0.5$  or  $\varepsilon \approx 2$  (Hervig et al., 2009a; Hervig and Gordley, 2010).

In this paper, the formation of noctilucent clouds consisting of non-spherical particles is studied in order to allow a direct comparison of lidar measurements to model data. This also allows predictions about the effects of particle shape on the formation of NLC layers.

## 2 Analysis methods

### 2.1 Model description

In this study, the size of noctilucent cloud particles is calculated using the Mesospheric Ice Microphysics And tranSport model (MIMAS), formerly named LIMA/ICE (Berger and Lübken, 2006; Lübken et al., 2009). MIMAS is a 3-D Lagrangian ice particle model for the polar mesosphere. Water vapor and an ensemble of 40 million condensation nuclei are transported by winds taken from an atmospheric circulation model, usually LIMA (Berger, 2008). When the ambient air is supersaturated, condensation nuclei are coated with ice. When they grow [into NLC](#) particle size, these ice particles sediment to lower altitudes within a few hours, where they eventually sublimate. The current version of MIMAS is described in detail in Kiliani (2014). More details about earlier model versions using dynamics from COMMA/IAP are found in Berger and von Zahn (2002), von Zahn and Berger (2003), Berger and von Zahn (2007), about MIMAS used with LIMA dynamics (LIMA/ICE) in Lübken et al. (2009, 2013).

## 2.2 Microphysics of non-spherical particles

In LIMA/ICE all ice particles are assumed to be spherical. For most purposes, this simplification is reasonable and widely used, for example in the CARMA NLC model (Megner, 2011; Merkel et al., 2009; Bardeen et al., 2010). For this study, cylindrical particle shape is used in addition to spherical particles. Pruppacher and Klett (1997) found a prevalence of cubic ice at the temperature and pressure range of NLC. More recent studies indicate a mixture of cubic and hexagonal ice (stacking disordered) (Murray et al., 2015). Direct measurements of tropospheric ice indicate strongly elongated or flattened shapes (Hobbs et al., 1974). To simplify the model representation of non-spherical shapes, we treat these as cylinders. We define a cylinder by its axis ratio  $\varepsilon = \frac{d}{h}$  and volume equivalent radius  $r = \sqrt[3]{\frac{3}{16}d^2 \cdot h}$ , with base diameter  $d$  and length of symmetry axis  $h$  (Fig. 1).  ~~$r$  is the radius of a sphere with equal volume to the cylinder.~~

Each model ice particle thus has a specified shape, in addition to a spatial coordinate and radius.  $\varepsilon$  is assumed to stay constant in time, i.e. the axis ratio does not change when cylindrical particles grow or sublimate (see Sect. 4). The particle shape modifies the growth rate  $\frac{dr}{dt}$ , this effect can be approximated as:

$$\left. \frac{dr}{dt} \right|_{\text{cylinder}} = \Phi_{drdt} \cdot \left. \frac{dr}{dt} \right|_{\text{sphere}} \quad (1)$$

where the factor  $\Phi_{drdt}$  depends on the particle shape, specifically the surface area  $S$  (e.g. Turco et al., 1982):

$$\Phi_{drdt} = \frac{S_{\text{cylinder}}(r, \varepsilon)}{S_{\text{sphere}}(r)} = \left( \frac{1}{\varepsilon} + \frac{1}{2} \right) \left( \frac{2\varepsilon}{3} \right)^{\frac{2}{3}} \quad (2)$$

The mass change rate of ice particles is proportional to the frequency of collisions with surrounding air molecules, and thus to the surface area  $S$ . Since  $S$  at a given volume is smallest for spheres, non-spherical shape makes particles grow or sublimate faster. Equation (1) is best suitable for larger particles: shape also modifies the Kelvin effect since that

depends on the mean particle curvature, but this effect is only pronounced for particles smaller than  $\approx 5$  nm and is currently not included in our simulations.

Elongated and flattened ice particles also sediment slower than spherical ones. While the speed of sedimentation depends on the particles' orientation, random orientation can be assumed for mesospheric ice: by way of their small size, rotational Brownian motion contributes a significant part of their thermal energy, equally distributed over all axes. Gadsden (1983) estimated this rotation at  $\approx 10^6$  Hz, so the randomization process is orders of magnitude faster than the MIMAS resolution of 90 s. The random particle orientation allows calculating an average vertical cross section for collisions with air molecules, which determines the sedimentation rate  $w_s$ . As this cross section increases for elongated and flattened particles for a given volume, needle- and disk-shaped particles fall slower than spheres:

$$\Phi_{\text{sedi}} = \frac{w_{\text{s,cylinder}}}{w_{\text{s,sphere}}} = \frac{\left(\frac{4}{9\varepsilon}\right)^{1/6} \cdot \left(1 + \frac{\pi}{8}\right)}{\frac{1}{4} \sqrt{3 + \frac{\pi}{2} + \varepsilon} \cdot \sqrt{2 + \frac{2}{\varepsilon} + \frac{\pi}{2}}}. \quad (3)$$

The correction factors  $\Phi_{\text{drdt}}$  and  $\Phi_{\text{sedi}}$  are shown in Fig. 2.  $\Phi_{\text{drdt}}$  and  $\Phi_{\text{sedi}}$  are around 2 and 0.5, respectively, for flattened particles with  $\varepsilon = 10$ . For elongated particles ( $\varepsilon = 0.1$ ), the values are closer to 1 than for  $\varepsilon = 10$ , indicating that “disc” shaped particles affect NLC microphysics more than “needle” shaped ones. Using a smaller range of particle shapes from  $\approx 0.3$  (needles) to 3 (discs) consistent with Hervig and Gordley (2010) leads to  $\Phi_{\text{drdt}} < 1.3$  and  $\Phi_{\text{sedi}} > 0.7$ . Both correction factors differ from 1 for  $\varepsilon = 1$ : cylindrical particles with equal diameter and height grow faster and fall slower than spherical particles. Also shown in Fig. 2,  $\left.\frac{dr}{dt}\right|_{\text{spheroid}} < \left.\frac{dr}{dt}\right|_{\text{cylinder}}$  for  $\varepsilon = 1$  values close to 1. Only oblate spheroids with  $\varepsilon > 4$  grow faster than flattened cylinders at the same axis ratio.

Finally, optical particle properties are also affected by particle shape: in the standard version of MIMAS, backscatter coefficients are calculated only for green light at 532 nm, assuming spherical shape. For this paper this is expanded to include randomly oriented cylindrical particles with variable axis ratios, calculated with the  $T$  matrix method (Mishchenko and Travis, 1998) at 355, 532 and 1064 nm. For typical particle sizes in NLC ( $< 100$  nm),

cylindrical ice [back](#) scatters light at 532 nm less efficiently than spherical particles with the same equivalent radius. For “needles” with  $\varepsilon = 0.1$  and large “discs” with  $\varepsilon = 10$ , the backscatter signal is less than half compared to spheres of the same volume (see Fig. 2). However, this does not necessarily imply that noctilucent clouds consisting of non-spherical particles are dimmer, as the growth and sedimentation mechanisms are affected by particle shape.

In summary, modeling of non-spherical particles is implemented by adjusting growth rate (Equation 1), fall speed (Equation 3), and Mie scatter coefficient using the T-matrix method.

### 2.3 Color ratios

Optical methods for determining particle properties typically involve analyzing scatter or extinction signals at several wavelengths or scattering angles (e.g. von Cossart et al., 1999; Hervig et al., 2009a; McClintock et al., 2009). Since the ALOMAR RMR-Lidar uses 1064 nm (IR) and 355 nm (UV) in addition to the visible 532 nm (Vis) [wavelengthline](#) (Baumgarten et al., 2010), backscatter coefficients for these wavelengths are implemented in MIMAS as well. Color ratios (CR) are defined as the relative scattering intensity of two wavelengths within the same sample volume. Unlike the backscatter signal ( $\beta$ ) at a single wavelength, a color ratio is determined entirely by the size and shape of the particles within the sample volume, but not by their number density.

The ALOMAR RMR-Lidar uses 532 nm as a reference signal. From three wavelengths, two independent color ratios can be derived:  $UV / Vis = \frac{\beta_{355 \text{ nm}}(r)}{\beta_{532 \text{ nm}}(r)}$  and  $IR / Vis = \frac{\beta_{1064 \text{ nm}}(r)}{\beta_{532 \text{ nm}}(r)}$ . [Figure 3](#) shows the values of both color ratios for randomly oriented cylinders, as a function of volume equivalent radius  $r$  and axis ratio  $\varepsilon$  in the parameter range  $r < 120$  nm and  $0.1 < \varepsilon < 10$ . [A uniform distribution of axial ratios \( \$0.1 < \varepsilon < 10\$ \) is used for the size retrievals as described in \(Baumgarten et al., 2007\).](#)

The color ratios of small particles asymptotically approach the limit of Rayleigh scattering. Since the refractive index of ice depends little on wavelength in the region of 355 to 1064 nm (e.g. Hale and Querry, 1973), the following approximation can be used:  $\beta_{\lambda}(r) \propto r^2 \left(\frac{r}{\lambda}\right)^4$  if

$r \ll \lambda$ , thus  $\frac{\beta_{355\text{ nm}}(r)}{\beta_{532\text{ nm}}(r)} \rightarrow \left(\frac{532\text{ nm}}{355\text{ nm}}\right)^4 \approx 5$ . Likewise for the IR / Vis ratio,  $\frac{\beta_{1064\text{ nm}}(r)}{\beta_{532\text{ nm}}(r)}$  converges to a value of about 0.06. This convergence is visible in Fig. 3 by the CR combinations of monodisperse distributions, where the lines for different axis ratios all intersect for small radii. Since small particles ( $r < 15\text{ nm}$ ) are difficult to detect by lidar in the first place, having similar color ratios makes it even more difficult to determine their size by optical methods. This makes analyzing particle shape using color ratios much more feasible for large particles, which primarily occur in bright ice clouds.

Also shown in Fig. 3), the UV / Vis ratio is highest for small particles, while at larger sizes it decreases rapidly up to a minimum at  $r \approx 100\text{ nm}$  (first UV resonance). In the size range 50 to 80 nm, the UV / Vis ratio also generally decreases with increasing  $\varepsilon$ . The UV / Vis ratio of needles ( $\varepsilon < 1$ ) is lower than for  $\varepsilon = 1$  particles with radii up to about 55 nm, higher for larger particles. For disc-shaped particles ( $\varepsilon = 10$ ), UV / Vis is smaller compared to  $\varepsilon = 1$  for  $r < 75\text{ nm}$  and larger for particles  $> 75\text{ nm}$ . The IR / Vis ratio shows a continuous rise toward larger radii for  $\varepsilon = 1$  particles, this increase is accelerating steeply around 100 nm. For all particles smaller than  $\approx 100\text{ nm}$ , IR / Vis is always smaller for  $\varepsilon = 1$  cylinders than for elongated or flattened particles. Up to radii around 70 nm, this increase is stronger for elongated ( $\varepsilon < 1$ ) particles.

The color ratio curves in Fig. 3 also intersect: in many cases, there are multiple combinations of particle size and shape that fit a given (i.e., measured) pair of UV / Vis and IR / Vis ratios. However, no particle shape causes lower IR / Vis ratios for a given UV / Vis than spherical particles. This makes the area to the left of the solid black line a “forbidden area”.

### 3 Results

#### 3.1 Comparison of modeled color ratios with observations

For comparison with model results we use 30 000 lidar measurements of color ratios observed in the period 1998 to 2014. In order to compare a wide range of NLC simulations with non-spherical shapes to these measurements, model simulations were conducted us-

ing background conditions from 5 days in mid-July of 2009, i.e. 120 time steps. ~~one month, i.e. 29 000 time steps from one month.~~ July 2009 was selected for compatibility to previous simulations (Kiliani et al., 2013). For the model data, 5 latitude bands from 67° N to 72° N were used, as well as 120 longitudinal bands (zonal model resolution is 3°).

The first simulation is the reference run with only spherical particle shape. Six model runs using very different distributions of non-spherical particles are also used, namely all shapes from highly elongated to very flat ( $0.1 < \varepsilon < 10$ ), moderately flat ( $1.1 < \varepsilon < 3.2$ ), moderately elongated ( $0.32 < \varepsilon < 0.87$ ), moderately elongated to flat ( $0.32 < \varepsilon < 3.2$ ), and moderately elongated to very flat ( $0.32 < \varepsilon < 5.65.8$ ) and ( $0.32 < \varepsilon < 10$ ). For all simulations with cylindrical particles, the initial particle shape is distributed uniformly in  $\log \varepsilon$ , for instance the simulation with ( $0.1 < \varepsilon < 10$ ) includes the same number of particles with ( $0.1 < \varepsilon < 0.2$ ) as ( $0.75 < \varepsilon < 1.5$ ) or ( $3 < \varepsilon < 6$ ). The shape distribution is discussed in more detail later, in Fig. 9. All simulations used exactly the same atmospheric conditions (e.g. temperature, H<sub>2</sub>O, wind).

For all these model simulations, ~~alla large number of~~ model grid volumes in the latitude range around ~~at the same latitude as~~ ALOMAR (69° N) are evaluated,  $\approx 1$  million in the peak backscatter range. ~~Since large particles are easier to distinguish using CR (Sect. 2.3), Since~~ the lidar statistic used here is restricted to strong NLC with  $\beta_{532} > 13 \times 10^{-10} \text{ m}^{-1} \text{ sr}^{-1}$ . ~~A,~~ an equivalent restriction is used for the modeled NLC, ~~which also removes the need for explicit altitude filtering.~~ From the resulting volumes containing strong NLC ( $\approx 100\,000$  per simulation), a distribution of modeled NLC color ratios is computed for each of the seven simulations.

Fig. ~~ure~~ 4 shows modeled color ratios from one of these simulations. Color ratios observed by lidar also include measurement uncertainties, which have to be simulated for the modeled NLC in order to compare color ratios directly. This is done by applying a Gaussian smoothing filter to the modeled CR, with a filter width determined by the lidar measurement uncertainties, i.e. 0.01 (IR / Vis) and 0.3 (UV / Vis), respectively. Fig. ~~ure~~ 4 shows the effect of the ~~smoothing filter on the Gaussian smoothing of~~ modeled color ratios for a simulation ~~containing both a combination of~~ needle- and disc-shaped particles. The unedited (mod-

eled) CR distribution for  $\beta > 13 \times 10^{-10} \text{ m}^{-1} \text{ sr}^{-1}$  covers a relatively narrow strip within the parameter space of IR / Vis and UV / Vis combinations, which roughly follows the line for spherical particles. For large particles (low UV / Vis) it diverges from the spherical particle line and becomes broader. As discussed in Sect. 2.3, the true CR distribution is sharply delimited by the spherical particle line: for ice particles smaller than  $\approx 100 \text{ nm}$ , this line constitutes a minimum IR / Vis ratio using standard Mie theory.

After applying the smoothing filter, the distribution becomes broader and resembles a drop-like shape, lying partially in the “forbidden area” to the left of the spherical particle curve. Because of the wedge shape of the true distribution, the probability density maximum (innermost, red isolines) is also shifted toward lower UV / Vis values.

In Fig. 5 we compare modeled color ratios for strong NLC in the spherical particle reference simulation to the lidar observations. The modeled distribution is drop-shaped like the one in Fig. 4, but with a steeper incline and aligned along the black curve for spherical particles.

The ALOMAR measured color ratios also form a drop shape, but both its alignment and the position of its mode (the probability density distribution maximum) differ considerably from the spherical model simulation. In particular, the simulated mode in UV / Vis is higher (by 0.9) and the one in IR / Vis is lower (by 0.015) compared to the lidar. Also, the measured CR include a long tail with IR / Vis ratios reaching up to 0.24, which is not adequately reproduced by the spherical particle simulation (max. IR / Vis: 0.13). In conclusion, using spherical ice particles produces color ratios which are not compatible with observations.

Figure 6 shows an extensive comparison of color ratios between the lidar data and six different cylindrical particle simulations and the lidar data, in the following referred to by their panel number in Fig. 6. Each panel includes a mean square deviation  $\chi^2$  to quantify the degree of similarity between simulation and measurements:

$$\chi^2 = \frac{1}{n} \sum_{i=1}^n (X_i - \hat{X}_i)^2 \quad (4)$$

where  $X_i$  is the probability density of the modeled color ratios and  $\hat{X}_i$  that of the lidar measured CRs in a given CR bin. Lower values of  $\chi^2$  indicate a better agreement.

The first simulation (a) represents a wide range of highly non-spherical cylinders ( $0.1 < \varepsilon < 10$ ). While this reproduces the measured distribution's tail adequately, the mode of the distribution is shifted towards higher IR / Vis to such an extent that  $\chi^2$  is even larger than for the spherical run. Figure 3 shows that highly elongated particles around 60 nm leave a characteristic signature in color ratios, in the form of strongly increased IR / Vis compared to spherical particles, accompanied by relatively high UV / Vis values. The position of the lidar measured CR mode thus counter-indicates the presence of such strongly needle-shaped ice particles to any great extent.

In the second model run (b), both disc- and needle-shaped particles are limited to moderate axis ratios ( $0.32 < \varepsilon < 3.2$ ). The comparison to the lidar data is much better with very similar distribution modes. The distribution tail is not reproduced very accurately, although considerably better than for the spherical reference run. This shape distribution is also consistent to satellite measurements with the SOFIE instrument (Hervig et al., 2009a; Hervig et al., 2010), who derived mean axis ratios around 2. However, SOFIE is not able to distinguish between needle- and disc-shaped particles with the same ratio of longest to shortest axis. For this reason two additional simulations were conducted, one with only flattened particles ( $1.1 < \varepsilon < 3.2$ ) and another using only elongated cylinders ( $0.32 < \varepsilon < 0.87$ ).

Neither of the simulations (c) and (d) are an improvement compared to (b). In particular, the distribution tail is largely unchanged with only a slight improvement for (d). For the needle-shaped cylinders (d), the distribution mode is shifted away from the measurements, while the color ratios of the flattened particle simulation (c) are stretched out along the UV / Vis axis more than the lidar data set. The preliminary conclusion is that a combination of discs and needles is needed to accurately replicate both the mode and the tail of the lidar measured distribution.

The remaining question is how to improve on (b) ( $0.32 < \varepsilon < 3.2$ ), primarily to get a better match for the distribution tail as in (a). The two simulations (e) and (f) include more

flattened ice particles while leaving the elongated part of the distribution unchanged compared to (b). The simulation (e) ( $0.32 < \varepsilon < 5.6$ ) shows even a slightly better match of the distribution modes as (b) while achieving a good approximation of the distribution tail. On the other hand, very highly flattened particles with  $\varepsilon$  up to 10 (Fig. 6f) cause an exaggerated distribution tail and a shifting of the mode at the same time. The reason for the good match with (e) can be seen in Fig. 3: the relatively rare very large disc-shaped particles  $> 80$  nm have much higher IR / Vis ratios compared to spheres or needles, which causes the tail and thus the drop shape of the color ratio distribution.

The analysis in Fig. 6 is qualitative to some extent because of its limited number of simulations, since the parameter space of possible particle shape distributions is much larger especially if non-uniform (e.g. Gaussian) distribution shapes are considered. A robust result is that cylindrical particles with axis ratios consistent with SOFIE (Hervig and Gordley, 2010) are also consistent with the ALOMAR lidar, that a mix of needle and disc shapes is required and that a slight emphasis on discs produces the best match.

### 3.2 Effects on ice layers

Since particle shape affects NLC microphysics in addition to optical cloud properties, the switch from spherical to cylindrical shape may affect the ice cloud morphology. Those effects are studied in this section, both in the average cloud morphology during mid-season, and in the size distribution during a single, bright NLC event.

In Fig. 7 we compare ~~observable parameters of simulated NLC layers~~  
~~brightness and altitude of the average NLC layer~~ at  $69^\circ$  N over a time period of one month (July of 2009). NLC consisting of non-spherical particles are up to 50 % brighter than those in the spherical particle simulation, resulting from both increased growth rates and reduced sedimentation compared to spheres (see Fig. 2). The brightness of the various non-spherical particle simulations are more similar: those favoring discs tend toward higher brightness than simulations with primarily needles, with differences in  $\beta$  of up to 30 %. This disparity is ~~caused by the stronger microphysical effects on growth and sedimentation for disc shapes as compared to needles~~  
~~most likely due to the slower sedimentation of needle shapes as compared~~

to discs (Fig. 2). The ice mass density of NLC in simulations with cylindrical particles is also up to  $\approx 30\%$  higher than in the spherical particle run. As for the backscatter coefficient, the increase in ice mass is larger for simulations with disc shaped cylinders than for needle shapes. The rather low values in average brightness and ice mass density result from the lack of a threshold. As minor changes in the mass density make some populations of clouds fall below the threshold in one simulation or the other, omitting a threshold gives more accurate comparisons for the different model runs.

The altitude of the NLC layer is much less affected by particle shape: all distributions have their brightness maximum within 100 m of each other, with the cylindrical particle simulations peaking at marginally higher altitude than the spherical reference run. Another parameter is the width of the mean ice layer, calculated as  $\Delta_z = \frac{\beta_{\text{int}}}{\beta_{\text{max}}}$ , where  $\beta_{\text{max}}$  is the maximum column-brightness and  $\beta_{\text{int}}$  the column integrated brightness at 532 nm (e.g. Fiedler et al., 2009). It varies between 1.53 km for spherical particles and 1.71 km for the distribution favoring highly flattened particles, see Table 1. Generally, the layer width increases with the axis ratios present in the shape distribution: the slower sedimentation and faster growth of non-spherical particles (especially disc-shaped) shifts the upper edge of the NLC region further up, while lower NLC edge and maximum altitude are less affected.

The altered particle shape also affects the particle size distribution and thus indirectly the backscatter signal in Fig. 7. In Fig. 8 we show the ice particle size and number density for a single strong NLC around  $69^\circ$  N at one time step (16 July 2009, 24:00 UT). In simulations with non-spherical ice particles, these grow  $\approx 5\text{--}10$  nm larger on average, depending on altitude and the simulation in question. Among the non-spherical shapes, those with the highest aspect ratios form the largest particles, and flattened particles grow noticeably larger than elongated ones. The width of the particle size distribution is also larger for non-spherical shapes in general, with a strong increase in the presence of very large particles ( $r > 80$  nm, not shown in Fig. 8).

On the other hand, the number of ice particles in the main layer of this strong NLC is generally lower for the non-spherical shapes compared to the spherical shapes, by 20–35%. As with particle size, the largest differences in number density are seen for simulations

including highly flattened particles. The increased size and decreased number density for non-spherical shape are linked to the availability of water vapor. For all simulations, the same initial H<sub>2</sub>O was used, this constrains the growth of NLC particles. The increased relative importance of turbulent transport compared to the (reduced) sedimentation rate results in a more effective differentiation of the ice layer into those particles growing visible ( $r > 20$  nm) and those staying at small size. For this reason, the larger particle size due to improved growth conditions for cylindrical ice is accompanied by a reduced number density in the NLC layer. Since the backscatter signal depends on particle size as  $r^5$  to  $r^{6, \mu=6}$ , NLC made of non-spherical particles are brighter than those with spherical particles in spite of the lower number density and reduced backscatter coefficient of single particles with the same equivalent radius.

Table 2 lists a number of additional microphysical parameters for the case of a strong cloud as shown in Fig. 8 for the (spherical) reference run and the various non-spherical particle simulations. The ice water content (IWC), defined as the column mass density of particles in the ice phase, shows a slight increase for cylindrical particle shapes, by 10–20%. High axis ratio particles appear to increase IWC more than only slightly non-spherical shapes. The small increase supports the earlier statement that a limited supply of water vapor results in larger particles but reduced number density **during strong growth conditions, i.e. when temperatures are low enough that a high fraction of the water vapor within the growth region is depleted by particle growth.** ~~if growth conditions improve.~~ IWC values for this event are generally high compared to satellite measurements (Hervig et al., 2009b; Hervig and Stevens, 2014), due to the choice of a very bright NLC. From Table 2 we see that the increase in backscatter signal for cylindrical particles is considerably weaker for this bright NLC example than for the statistic in Table 1. Only  $\beta_{\text{int}}$  is consistently larger, similar to the results when analyzing all NLC. As for the statistic in Table 1, flattened particles lead to brighter ice clouds, **by 15-25 % compared to the spherical simulation.**

Finally, Fig. 9 shows the development of ice particles within the six simulations with cylindrical ice particles. When counting all particles, the uniform **initial** distribution shapes (see Sect. 3.1) within the respective  $\varepsilon$  limits are evident in all panels, minor deviations are due to

statistical variability caused by the random number generator. However, when counting only particles larger than specific radius thresholds, the resulting distributions are no longer uniform, but constitute a U shape: strongly non-spherical particles are considerably more common than those with  $\varepsilon$  close to 1 if only large particles are considered. For the simulation (a) with ( $0.1 < \varepsilon < 10$ ), highly flattened particles ( $\varepsilon = 10$ ) are around 70% more common than  $\varepsilon = 1$  particles, if the radius threshold is set at 5 nm.  $\varepsilon = 10$  is 3 times more common than  $\varepsilon = 1$  for particles with  $r > 10$  nm and nearly 6 times more common for  $r > 20$  nm. This imbalance is smaller but still distinct for elongated or more moderately flattened cylinders. It also appears to be largest for size thresholds around 20 nm, since the imbalance is slightly smaller for a threshold of 40 nm (visible NLC particles).

These differences in Fig. 9 are much larger than those between simulations in Figs. 7 and 8: with their larger surface to volume ratio, strongly non-spherical particles outperform low  $\varepsilon$  particles in growing to large size in a common volume. This is observed both for elongated and flattened high  $\varepsilon$  particles, but most pronounced for the flattened (disc-shaped) case. The prevalence of high axis ratios among large particles is most likely due to the increased growth rates, with the reduced fall speed contributing slightly at most. Otherwise we would expect the center of the U-shape shifted to elongated particles, like for the correction factor  $\Phi_{\text{sedi}}$ , see Fig. 2. Shape inhomogeneities in the general particle distribution tend to get amplified within the NLC layer: Fig. 9 includes the average axis ratio  $\langle \varepsilon \rangle$  for each radius threshold, calculated using  $\frac{1}{\varepsilon}$  for  $\varepsilon < 1$ .  $\langle \varepsilon \rangle$  is shifted to higher values when only large ( $r > 20$  nm) particles are considered, by  $\approx 0.1$  in simulations (b), (c), and (d) and by 1.2 and 1.4 in simulations (a) ( $0.1 < \varepsilon < 10$ ) and (f) ( $0.32 < \varepsilon < 10$ ), respectively. This helps to explain the large effects on the optical NLC properties in Sect. 3.1 seen for simulations including highly aspheric particles. For simulation (e) ( $0.32 < \varepsilon < 5.6$ ), where we find the best agreement to the ALOMAR lidar, the  $\langle \varepsilon \rangle$  value of 2.8 for  $r > 20$  nm is more suitable for comparing mean axis ratios to SOFIE satellite measurements than the lower value 2.4 for the initial distribution since the backscatter signal is caused by large ice particles. Our analysis thus yields a somewhat higher estimate for mean axis ratio than the value of 2.0 by Hervig and Gordley (2010).

#### 4 Discussion and conclusions

Size and shape of noctilucent cloud particles have long been an important topic in characterizing ice formation in the upper mesosphere region. While the particle size has been studied extensively, spherical shape is commonly assumed for mesospheric ice particles, especially in model studies. In this paper, several distributions of non-spherical ice particles are studied. To limit computational complexity, particles are assumed to be rotationally symmetric, in particular cylindrical shaped, and particle shape is further assumed to stay constant in time. ~~This last assumption was chosen as a simple way to treat axis ratios effects on the microphysics. Uniform condensation on an elongated or flattened particle would continually decrease its axial ratio during growth. On the other hand the crystalline structure of ice or particle charge could counteract this to increase axial ratios. An implementation of all effects would require much more complex microphysics, which is beyond the scope of the paper.~~

The optical properties of these model ice particles are compared with measurements: while a lidar is capable of measuring shape information directly through depolarization, ~~this is not done routinely is difficult in practice since the effect is so small that such measurements require nearly perfect conditions~~ (Baumgarten et al., 2002). ~~The depolarization approach is thus not pursued further, since~~ Using the relative strength of the scatter signal in three different wavelengths (color ratios) gives a **larger and** more robust data set for comparison with models.

~~(Rapp et al., 2007) found that~~The color ratios from NLC as measured by lidar do not match the model simulation well if it is assumed that particles are of spherical shape. ~~For 11 color ratio measurements in 1998 by von Cossart et al. (1999) they found that needles with axial ratios of 1/5 or plates with axial ratio of 7 explain the observations.~~

With an extended dataset of about 30000 color ratio measurements and improved modeling ~~t~~The agreement is much better for simulations with cylindrical particles, particularly if both elongated and flattened particles are included. The simulation ~~most~~**best** consistent with the lidar ( $0.32 < \varepsilon < 5.6$ ) includes  $\approx 60\%$  more discs ( $\varepsilon > 1.25$ ) than needles ( $\varepsilon < 0.8$ ),

with a mean  $\varepsilon$  of 2.8. From the good agreement of color ratios we infer that the ice clouds observed by lidar have a distribution of both particle size and shape very similar to the model run.

The model simulations with cylindrical particles generally produce brighter ice layers, mainly because their shape slows sedimentation compared to spherical particles and thus enables them to grow to larger sizes. Mean NLC brightness ( $\beta_{532\text{nm}}$ ) is also increased by up to 50 %, yet this affects weaker ice clouds more than strong NLC: comparing various simulations for the case of a strong NLC, the upper end of the particle size distribution is shifted towards considerably larger particles for the non-spherical case. The mean size is 5–10 nm larger for the non-spherical particles, accompanied by a broadening of the size distribution. Since particle number densities for the non-spherical particle simulations are lower, the brightness increase is less than would be expected from particle size alone. Simulations using non-spherical particles **also feature only a modest increase in ice mass (IWC) of up to 30–20 %, reduced to 10–20 % when considering only strong ice clouds.**

Using cylindrical instead of spherical particle shape in NLC modeling makes the simulated optical cloud properties consistent with lidar and satellite observations. The effects on NLC microphysics are less pronounced: cylindrical NLC particles are slightly larger, but the corresponding increase in ice water content and cloud brightness is partly compensated by reduced number densities.

To conclude, the effects of using non-spherical particles on optical NLC properties such as color ratios or scattering angles (for satellites) are considerable and important for comparing simulations to measurements.

*Acknowledgements.* This research was sponsored by the German Federal Ministry of Education and Research through the Role Of the Middle atmosphere In Climate (ROMIC) project Trends In the Middle Atmosphere (TIMA), grant number 01LG1210A. We gratefully acknowledge the European Center for Medium-Range Weather Forecasts (ECMWF) for providing the ERA-40 reanalysis data used in the simulations.

## References

- Bardeen, C. G., Toon, O. B., Jensen, E. J., Hervig, M. E., Randall, C. E., Benze, S., Marsh, D. R., and Merkel, A.: Numerical simulations of the three-dimensional distribution of polar mesospheric clouds and comparisons with Cloud Imaging and Particle Size (CIPS) experiment and the Solar Occultation For Ice Experiment (SOFIE) observations, *J. Geophys. Res.*, 115, D10204, doi:10.1029/2009JD012451, 2010.
- Baumgarten, G. and Thomas, G. E.: The importance of ice particle shape on UV measurements of polar mesospheric clouds: SBUV/2 observations, *J. Atmos. Sol.-Terr. Phys.*, 68, 78–84, doi:10.1016/j.jastp.2005.08.007, 2006.
- Baumgarten, G., Fricke, K. H., and von Cossart, G.: Investigation of the shape of noctilucent cloud particles by polarization lidar technique, *Geophys. Res. Lett.*, 29, 8-1–8-4, doi:10.1029/2001GL013877, 2002.
- Baumgarten, G., Fiedler, J., and von Cossart, G.: The size of noctilucent cloud particles above ALOMAR (69N,16E): Optical modeling and method description, *Adv. Space Res.*, 40, 772–784, doi:10.1016/j.asr.2007.01.018, 2007.
- Baumgarten, G., Fiedler, J., and Rapp, M.: On microphysical processes of noctilucent clouds (NLC): observations and modeling of mean and width of the particle size-distribution, *Atmos. Chem. Phys.*, 10, 6661–6668, doi:10.5194/acp-10-6661-2010, 2010.
- Berger, U.: Modeling of middle atmosphere dynamics with LIMA, *J. Atmos. Sol.-Terr. Phys.*, 70, 1170–1200, doi:10.1016/j.jastp.2008.02.004, 2008.
- Berger, U. and Lübken, F.-J.: Weather in mesospheric ice layers, *Geophys. Res. Lett.*, 33, L04806, doi:10.1029/2005GL024841, 2006.
- Berger, U. and von Zahn, U.: Icy particles in the summer mesopause region: three-dimensional modeling of their environment and two-dimensional modeling of their transport, *J. Geophys. Res.*, 107, 1366, doi:10.1029/2001JA000316, 2002.
- Berger, U. and von Zahn, U.: Three-dimensional modeling of the trajectories of visible noctilucent cloud particles: an indication of particle nucleation well below the mesopause, *J. Geophys. Res.*, 112, D16204, doi:10.1029/2006JD008106, 2007.
- Eremenko, M. N., Zasetsky, S. V. P. A. Y., Karlsson, B., Rinsland, C. P., Llewellyn, E. J., and Sloan, J. J.: Shape and composition of PMC particles derived from satellite remote sensing measurements, *Geophys. Res. Lett.*, 32, L16S06, doi:10.1029/2005GL023013, 2005.

- Fiedler, J., Baumgarten, G., and Lübken, F.-J.: NLC observations during one solar cycle above ALOMAR, *J. Atmos. Sol.-Terr. Phys.*, 71, 424–433, doi:10.1016/j.jastp.2008.11.010, 2009.
- Gadsden, M.: A note on the orientation and size of noctilucent cloud particles, *Tellus B*, 35, 73–75, doi:10.1111/j.1600-0889.1983.tb00009.x, 1983.
- Hale, G. M. and Querry, M. R.: Optical constants of water in the 200-nm to 200-micrometer wavelength region, *Appl. Optics*, 12, 555, doi:10.1364/AO.12.000555, 1973.
- Hervig, M. E. and Gordley, L. L.: Temperature, shape, and phase of mesospheric ice from Solar Occultation for Ice Experiment observations, *J. Geophys. Res.*, 115, D15208, doi:10.1029/2010JD013918, 2010.
- Hervig, M. E. and Stevens, M. H.: Interpreting the 35 year SBUV PMC record with SOFIE observations, *J. Geophys. Res.*, 119, 12689, doi:10.1002/2014JD021923, 2014.
- Hervig, M. E., Gordley, L. L., Stevens, M. H., Russell III, J. M., Bailey, S. M., and Baumgarten, G.: Interpretation of SOFIE PMC measurements: cloud identification and derivation of mass density, particle shape, and particle size, *J. Atmos. Sol.-Terr. Phys.*, 71, 316–330, doi:10.1016/j.jastp.2008.07.009, 2009a.
- Hervig, M. E., Stevens, M. H., Gordley, L. L., Deaver, L. E., Russell, J. M., and Bailey, S. M.: Relationships between polar mesospheric clouds, temperature, and water vapor from Solar Occultation for Ice Experiment (SOFIE) observations, *J. Geophys. Res.*, 114, D20203, doi:10.1029/2009JD012302, 2009b.
- Hobbs, P. V., Chang, S., and Locatelli, J. D.: The dimensions and aggregation of ice crystals in natural clouds, *J. Geophys. Res.*, 79, 2199–2206, doi:10.1029/JC079i015p02199, 1974.
- Holton, J. R.: The influence of gravity wave breaking on the general circulation of the middle atmosphere, *J. Atmos. Sci.*, 40, 2497–2507, doi:10.1175/1520-0469(1983)040<2497:TIOGWB>2.0.CO;2, 1983.
- Kiliani, J.: 3-D Modeling of Noctilucent Cloud Evolution and Relationship to the Ambient Atmosphere, PhD thesis, Universität Rostock, Rostock, Germany, 2014.
- Kiliani, J., Baumgarten, G., Lübken, F.-J., Berger, U., and Hoffmann, P.: Temporal and spatial characteristics of the formation of strong noctilucent clouds, *J. Atmos. Sol.-Terr. Phys.*, 104, 151–166, doi:10.1016/j.jastp.2013.01.005, 2013.
- Lübken, F., Berger, U., and Baumgarten, G.: Stratospheric and solar cycle effects on long-term variability of mesospheric ice clouds, *J. Geophys. Res.*, 114, D00106, doi:10.1029/2009JD012377, 2009.

- Lübken, F.-J., Berger, U., Kiliani, J., Baumgarten, G., and Fiedler, J.: Solar variability and trend effects in mesospheric ice layers, in: *Climate and Weather of the Sun-Earth System (CAWSES)*, edited by: Lübken, F.-J., Springer, Dordrecht, 317–338, doi:10.1007/978-94-007-4348-9\_18, 2013.
- McClintock, W. E., Rusch, D. W., Thomas, G. E., Merkel, A. W., Lankton, M. R., Drake, V. A., Bailey, S. M., and Russell, III, J. M.: The cloud imaging and particle size experiment on the Aeronomy of Ice in the mesosphere mission: instrument concept, design, calibration, and on-orbit performance, *J. Atmos. Sol.-Terr. Phys.*, 71, 340–355, doi:10.1016/j.jastp.2008.10.011, 2009.
- Megner, L.: Minimal impact of condensation nuclei characteristics on observable Mesospheric ice properties, *J. Atmos. Solar-Terr. Phys.*, 73, 2184–2191, doi:10.1016/j.jastp.2010.08.006, 2011.
- Merkel, A. W., Marsh, D. R., Gettelman, A., and Jensen, E. J.: On the relationship of polar mesospheric cloud ice water content, particle radius and mesospheric temperature and its use in multi-dimensional models, *Atmos. Chem. Phys.*, 9, 8889–8901, doi:10.5194/acp-9-8889-2009, 2009.
- Mishchenko, M. I. and Travis, L. D.: Capabilities and limitations of a current FORTRAN implementation of the T-matrix method for randomly oriented, rotationally symmetric scatterers, *J. Quant. Spectrosc. Ra.*, 60, 309–324, doi:10.1016/S0022-4073(98)00008-9, 1998.
- Murray, B. J., Malkin, T. L., and Salzmann, C. G.: The crystal structure of ice under mesospheric conditions, *J. Atmos. Sol.-Terr. Phys.*, 127, 78–82, doi:10.1016/j.jastp.2014.12.005, 2015.
- Pruppacher, H. R. and Klett, J. D.: *Microphysics of Clouds and Precipitation*, Kluwer Academic Publishers, Dordrecht, 1997.
- Rapp, M., Thomas, G. E., and Baumgarten, G.: Spectral properties of mesospheric ice clouds: evidence for non-spherical particles, *Geophys. Res. Lett.*, 112, D03211, doi:10.1029/2006JD007322, 2007.
- Turco, R. P., Toon, O. B., Whitten, R. C., Keesee, R. G., and Hollenbach, D.: Noctilucent clouds – simulation studies of their genesis, properties and global influences, *Planet. Space Sci.*, 30, 1147–1181, doi:10.1016/0032-0633(82)90126-X, 1982.
- von Cossart, G., Fiedler, J., and von Zahn, U.: Size distributions of NLC particles as determined from 3-colour observations of NLC by ground-based Lidar, *Geophys. Res. Lett.*, 26, 1513–1516, doi:10.1029/1999GL900226, 1999.
- von Zahn, U. and Berger, U.: Persistent ice cloud in the midsummer upper mesosphere at high latitudes: three-dimensional modeling and cloud interactions with ambient water vapor, *J. Geophys. Res.*, 108, 8451, doi:10.1029/2002JD002409, 2003.

**Table 1.** Mean values for MIMAS NLC brightness North of 60at69° N using different particle shape distributions.

Particle shape	$\beta_{\max}$ [ $10^{-10} \text{ m}^{-1} \text{ sr}^{-1}$ ]	$\beta_{\text{int}}$ [ $10^{-7} \text{ sr}^{-1}$ ]	$\Delta_z$ [km]
Spherical	6.26	9.58	1.53
Cylindrical			
0.1 < $\varepsilon$ < 10	8.53	14.44	1.69
0.32 < $\varepsilon$ < 3.2	8.20	13.01	1.59
1.1 < $\varepsilon$ < 3.2	9.06	14.38	1.59
0.32 < $\varepsilon$ < 0.87	7.41	11.67	1.57
0.32 < $\varepsilon$ < 5.6	8.86	14.37	1.62
0.32 < $\varepsilon$ < 10	9.46	16.21	1.71

**Table 2.** Microphysical parameters for the same strong NLC as in Fig. 8, compared between simulations with different particle shape distributions. The altitude of maximum brightness used for  $n_{\max}$ ,  $r_{\max}$  and  $\sigma(r_{\max})$  is 82–83 km, and only particles larger than 15 nm are considered for all parameters.

Particle shape	$n_{\max}$ [cm <sup>-3</sup> ]	$r_{\max}$ [nm]	$\sigma(r_{\max})$ [nm]	$\bar{r}$ [nm]	IWC [g km <sup>-2</sup> ]	$\beta_{\max}$ [10 <sup>-10</sup> m <sup>-1</sup> sr <sup>-1</sup> ]	$\beta_{\text{int}}$ [10 <sup>-7</sup> sr <sup>-1</sup> ]
Spherical	151.3	57.6	11.5	31.7	266	63.7	67.3
Cylindrical							
0.1 < $\varepsilon$ < 10	122.4	64.2	14.2	35.0	328	59.5	73.3
0.32 < $\varepsilon$ < 3.2	105.9	63.6	13.6	32.7	293	66.8	77.0
1.1 < $\varepsilon$ < 3.2	99.8	67.4	13.6	32.9	305	73.8	90.5
0.32 < $\varepsilon$ < 0.87	133.0	60.8	13.7	32.7	299	64.8	74.6
0.32 < $\varepsilon$ < 5.6	98.3	66.4	14.5	33.4	309	65.1	81.9
0.32 < $\varepsilon$ < 10	108.2	67.4	14.2	35.3	338	63.1	83.7

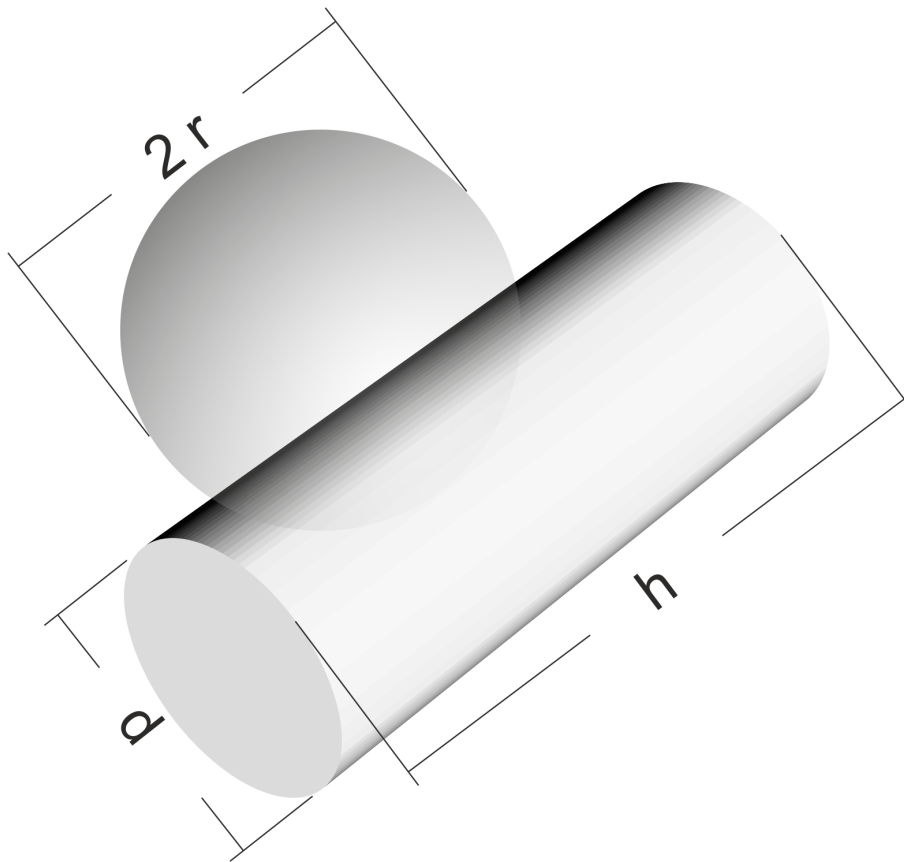


**Figure 1.** Nomenclature used for cylindrical ice particles.

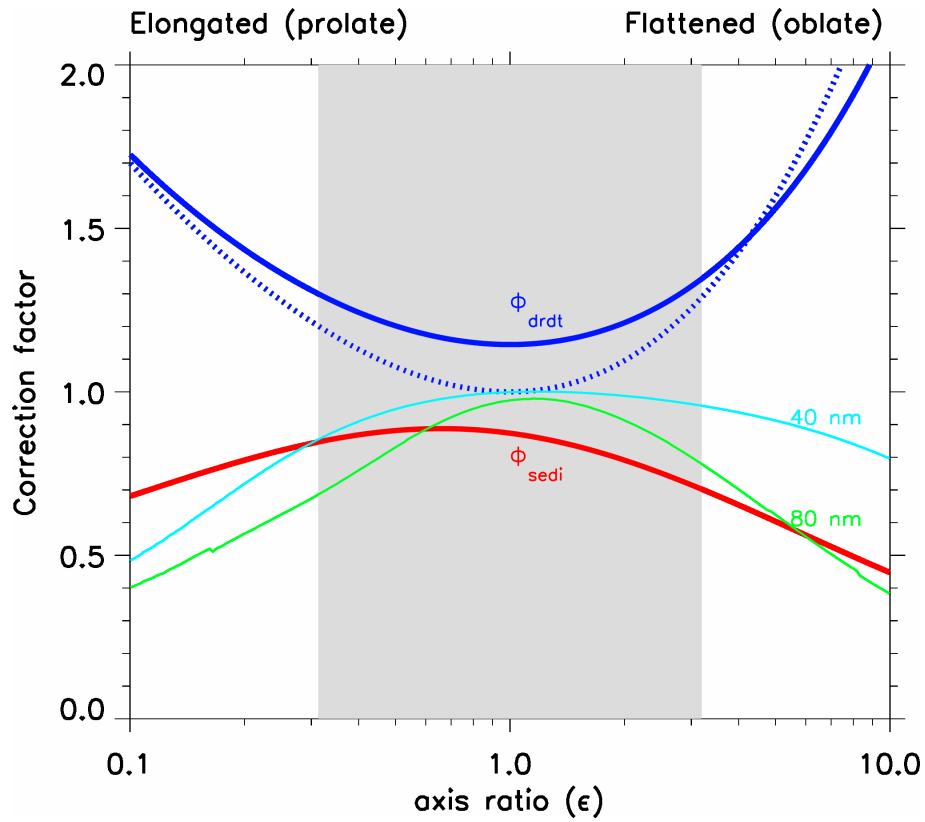


**Figure 2.** Correction factors  $\Phi_{drdt}$  for particle growth and  $\Phi_{sedi}$  for sedimentation of cylinders relative to growth and sedimentation of spheres. The dotted blue line shows  $\Phi_{drdt}$  for spheroid particle shape. Thin lines show the backscatter signal (532 nm) ratio of same volume cylinders to spheres for equivalent radii of 40 and 80 nm. Shading indicates the  $\epsilon$  limits of moderately elongated or flattened particles consistent with satellite measurements (Hervig and Gordley, 2010).

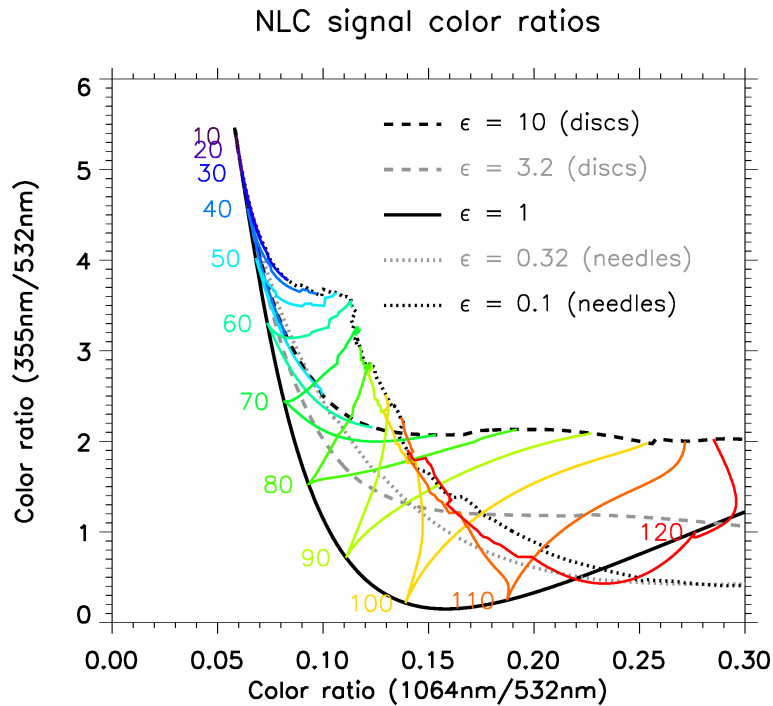


**Figure 3.** Combinations of color ratios UV / Vis (355/532 nm) and IR / Vis (1064/532 nm) for different particle equivalent radii  $r$  and axis ratios  $\epsilon$ , as calculated from Mie theory for cylindrical particles. Colored solid lines show constant  $r$  with variable  $\epsilon$ , the equivalent radius in nm is shown by the numbers near the  $\epsilon = 1$  position (the line inflection is caused by very small  $\frac{d\beta}{d\epsilon}$  at  $\epsilon = 1$ ). Line oscillations, mainly along the  $\epsilon < 1$  branch, stem from rounding errors in the Mie scattering tables. The grey scale lines (dotted/dashed) show variable  $r$  for fixed axis ratios, including cylinders with  $\epsilon = 1$  for the solid black line.

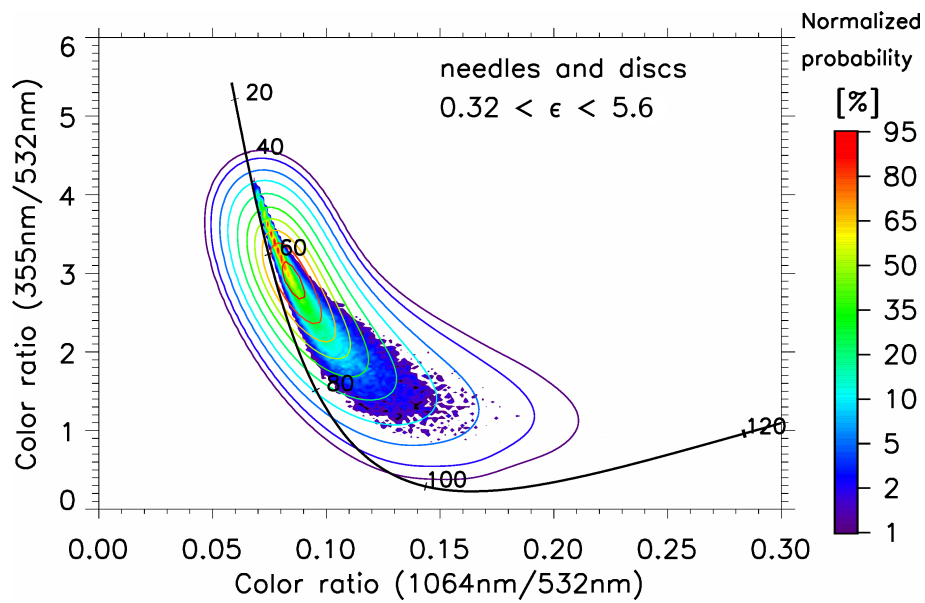


**Figure 4.** Filled contours: modeled distribution of color ratios for one NLC simulation with cylindrical particles, normalized to 100 % for the most common CR combination. Contour lines: same distribution after applying a Gaussian smoothing filter determined by the uncertainty of lidar measured color ratios. Black line: color ratios for spherical particles, numbers show CR for particular spherical particle radii. *These are very similar but not identical to the  $\epsilon = 1$  cylinders in, see Fig. 3.*

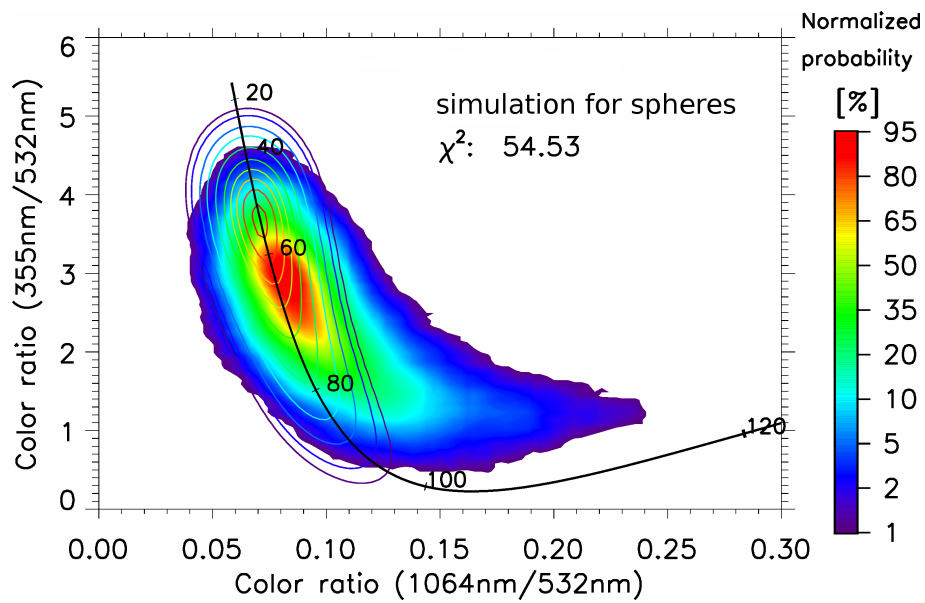


**Figure 5.** Filled contours: measured multi-year statistic of color ratio distribution observed by ALO-MAR RMR-Lidar for strong NLC ( $\beta > 13 \times 10^{-10} \text{ m}^{-1} \text{ sr}^{-1}$ ). Contour lines: modeled CR distribution for spherical particle simulation from  $67^\circ \text{ N}$  to  $72^\circ \text{ N}$  with simulated measurement error.  $\chi^2$  refers to the difference between model and measurements, see Fig 6. All distributions are normalized to 100% for their respective probability density maximum.

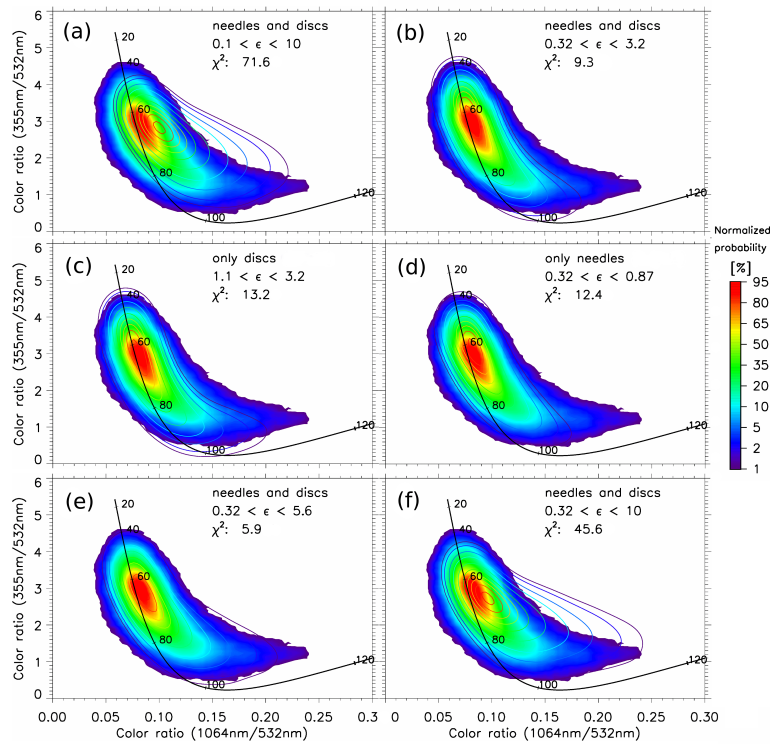


**Figure 6.** Filled contours, all panels: lidar CR statistic as in Fig. 5. Contour lines: modeled color ratio distribution including simulated measurement errors for six different cylindrical particle shape distributions. All distributions are normalized to 100 % for their respective maximum.  $\chi^2$  values are calculated by averaging the squared deviations between model and observation (in %) over the plot area,  $0 < UV / Vis < 6$  and  $0 < IR / Vis < 0.3$ .

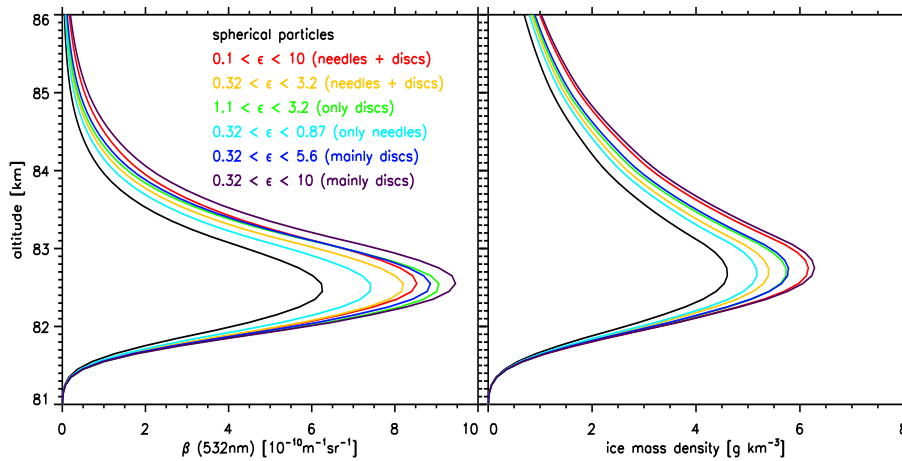


**Figure 7.** Average NLC parameters Average backscatter coefficient (532 nm) North of 60° Nat 69°N during July of 2009, from the reference simulation (spherical particles) and 6 sensitivity runs with different distributions of cylindrical particles. Left panel: backscatter coefficient (532 nm), right panel: ice mass density ( $\text{g} \cdot \text{km}^{-3}$ ). No threshold is used, i.e. zero values are included in the average.

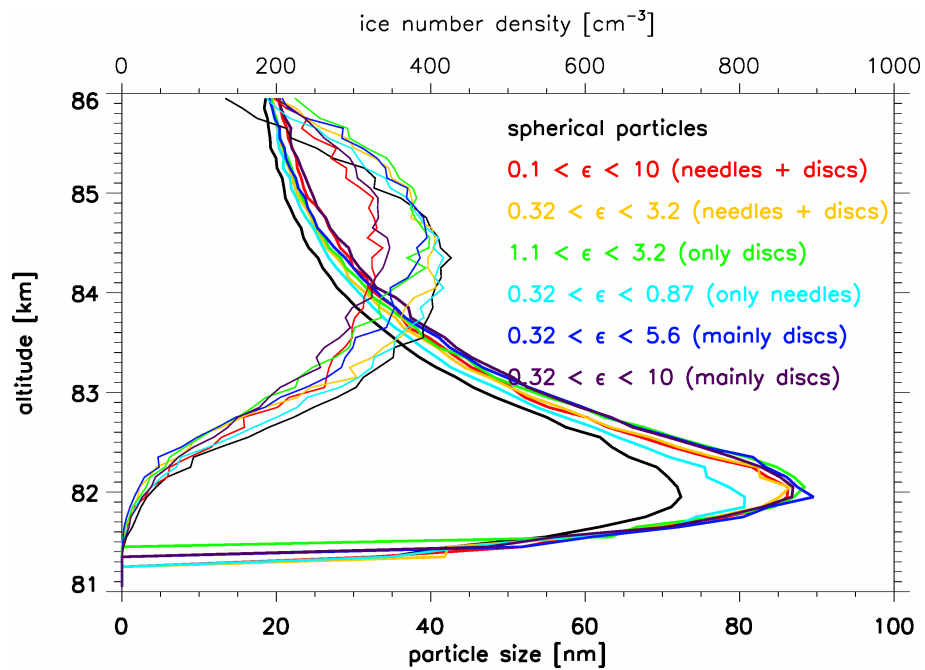


**Figure 8.** Simulated volumeNLC-particle equivalent radius and number density for a bright NLC event between 135–150° E, 67–72° N on 16 July, 24:00 UT, with different shape distributions. Only particles > 15 nm are included in the average of size and number density.

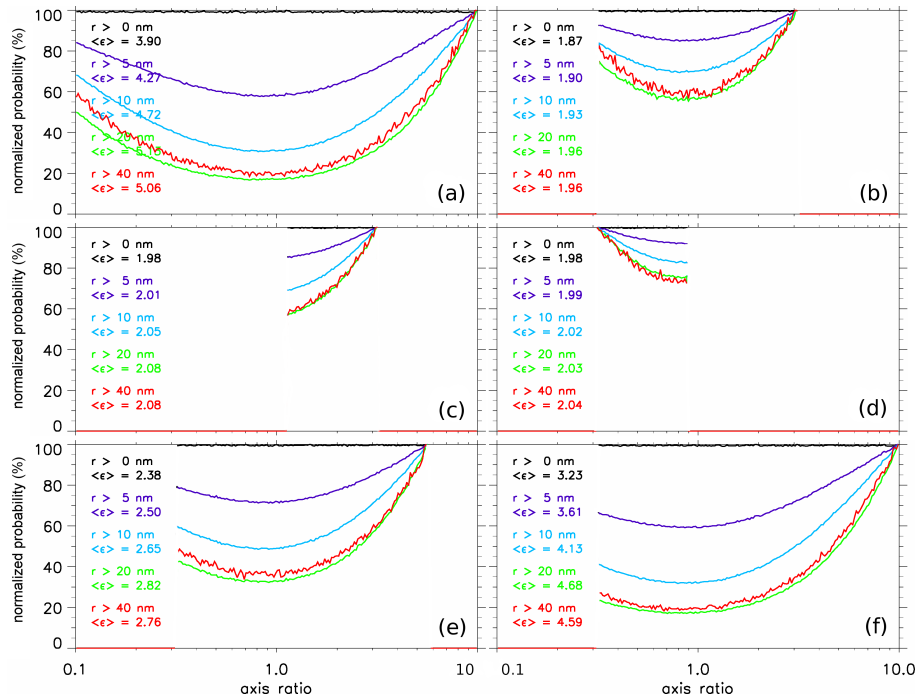


**Figure 9.** Shape distribution of simulations with non-spherical particles on 16 July, 24:00 UT, panels (a) to (f) are arranged analogous to Fig. 6. Black lines are the initial ( $\log \epsilon$ ) uniform distributions including all ice particles, colored lines show shape distributions for particles larger than a given threshold. For each radius threshold the distributions are individually normalized to the most common particle shape, and mean  $\epsilon$  values ( $\langle \epsilon \rangle$ ) are calculated using  $\frac{1}{\epsilon}$  for  $\epsilon < 1$ .